Environmental Science Processes & Impacts

ROYAL SOCIETY OF CHEMISTRY

PAPER

View Article Online
View Journal | View Issue

Check for updates

Cite this: *Environ. Sci.: Processes Impacts*, 2024, **26**, 1999

Modeling of mercury deposition in India: evaluating emission inventories and anthropogenic impacts†

Chakradhar Reddy Malasani,[ab] Basudev Swain, *[c] Ankit Patel,[ab] Yaswanth Pulipatti,[d] Nidhi L. Anchan, [ab] Amit Sharma,[e] Marco Vountas,[c] Pengfei Liu[f] and Sachin S. Gunthe *[ab]

Received 31st May 2024
Accepted 16th September 2024

DOI: 10.1039/d4em00324a

rsc.li/espi

Mercury (Hg), a ubiquitous atmospheric trace metal posing serious health risks, originates from natural and anthropogenic sources. India, the world's second-largest Hg emitter and a signatory to the Minamata Convention, is committed to reducing these emissions. However, critical gaps exist in our understanding of the spatial and temporal distribution of Hg across the vast Indian subcontinent due to limited observational data. This study addresses this gap by employing the GEOS-Chem model with various emission inventories (UNEP2010, WHET, EDGAR, STREETS, and UNEP2015) to simulate Hg variability across the Asian domain, with a specific focus on India from 2013 to 2017. Model performance was evaluated using ground-based GMOS observations and available literature data. Emission inventory performance varied across different observational stations. Hence, we employed ensemble results from all inventories. The maximum relative bias for Total Gaseous Mercury (TGM) and Gaseous Elemental Mercury (GEM; Hg^0) concentrations is about ±20%, indicating simulations with sufficient accuracy. Total Hg wet deposition fluxes are highest over the Western Ghats and the Himalayan foothills due to higher rainfall. During the monsoon, the Hg wet deposition flux is about 65.4% of the annual wet deposition flux. Moreover, westerly winds cause higher wet deposition in summer over Northern and Eastern India. Total Hg dry deposition flux accounts for 72–74% of total deposition over India. Hg^0 dry deposition fluxes are higher over Eastern India, which correlates strongly with the leaf area index. Excluding Indian anthropogenic emissions from the model simulations resulted in a substantial decrease (21.9% and 33.5%) in wet and total Hg deposition fluxes, highlighting the dominant role of human activities in Hg pollution in India.

Environmental significance

Mercury, a toxic pollutant that accumulates in the food chain and can cause serious health problems, must be closely monitored in India. Being the world's second-largest anthropogenic Hg emitter, India has signed a global treaty (the Minamata Convention) to reduce it. This study utilizes the GEOS-Chem model (2013–2017) to reveal the seasonal and spatial patterns of Hg deposition in India. Significant wet deposition fluxes occur in the biodiverse Western Ghats during the monsoon season, highlighting potential ecological threats. A strong link between vegetation and dry deposition suggests a role of plant cover. Notably, Indian anthropogenic emissions contribute substantially to Hg deposition fluxes (21.9% and 33.5% of wet and dry deposition, respectively), underlining the further studies and urgency for emission control strategies.

1 Introduction

Mercury, a toxic pollutant, can bioaccumulate in the food chain and significantly impact human health, causing neurological and cardiovascular problems.[1,2] It enters the atmosphere from both natural and anthropogenic emission sources.[3] The natural sources of mercury include mineral mercury deposits, volcanoes, and geothermal sources.[4] Anthropogenic sources include

---

[a] Enviromental Engineering Division, Department of Civil Engineering, Indian Institute of Technology Madras, Chennai, India. E-mail: s.gunthe@iitm.ac.in

[b] Centre for Atmospheric and Climate Sciences, Indian Institute of Technology Madras, Chennai, India

[c] Institute of Environmental Physics, Department of Physics, University of Bremen, Bremen, Germany. E-mail: basudev@iup.physik.uni-bremen.de

[d] Hydraulics and Water Resources Engineering Division, Department of Civil Engineering, Indian Institute of Technology Madas, Chennai, India

[e] Department of Civil and Infrastructure Engineering, Indian Institute of Technology Jodhpur, Jodhpur, India

[f] School of Earth and Atmospheric Sciences, Georgia Institute of Technology, Atlanta, GA, USA

† Electronic supplementary information (ESI) available. See DOI: **https://doi.org/10.1039/d4em00324a**

fossil fuel combustion, mineral ore processing, waste incineration, and intentional uses like industrial processes and artisanal gold mining.[5] Additionally, biomass burning and the re-release of previously deposited mercury from soil, water, and vegetation can have contributions from both natural and anthropogenic sources.[3] Mercury exists in various forms in the atmosphere: Gaseous Elemental Mercury (GEM, Hg^0), Reactive Gaseous Mercury (RGM, Hg^{II}_g), and Particulate Bound Mercury (PBM, Hg^{II}_p).[6] The different forms of mercury have distinct physical and chemical properties that significantly affect their transport, transformation, and removal. GEM, with its longer atmospheric lifetime, can travel vast distances across continents and is primarily removed by dry deposition. Short-lived RGM and PBM are readily removed through both wet and dry deposition processes.[7]

Mercury (Hg) poses a significant threat due to its toxicity and detrimental impacts on human health and ecosystems. Spatio-temporal variability studies are crucial, particularly in densely populated countries like India. India is the world's second-largest atmospheric Hg emitter,[8,9] and projections suggest an increase in emissions without stringent control measures.[10,11] Recognizing the global scope of Hg pollution and its health consequences, the Minamata Convention (**https://minamataconvention.org/en**) was adopted in 2017. India ratified the convention in 2018, committing to reduce atmospheric Hg emissions and overall environmental pollution.

While countries like Canada, the USA, and Europe have established extensive mercury monitoring networks in the past three decades, India lacks such a comprehensive system to map the spatio-temporal distribution of mercury across its vast subcontinent. Existing data rely on estimates rather than real-time measurements from various emission sources.[12] Further compounding this challenge, India's unique tropical and subtropical climate is shaped by diverse landscapes like the Himalayas, the Thar Desert, and the ocean. Furthermore, the distinct monsoon system in India is likely a key driver of Hg transport.[13,14] Understanding Hg emission sources, atmospheric distribution, transformation, and fate is essential for implementing effective mitigation strategies. Therefore, establishing an India-specific understanding of Hg sources and sinks is critical.

Most studies on mercury pollution in India have focused on measuring atmospheric Hg levels near contaminated sites, which limits our understanding of mercury pollution on a national scale. These localized measurements provide valuable insights, but they do not represent the diverse environmental conditions and emission sources across the vast subcontinent. Moreover, the lack of comprehensive observational data and modelling studies has hindered our ability to assess mercury pollution on a national scale. Studies have shown elevated mercury levels in the blood, urine, and breast milk of residents and workers near an integrated steel plant in Bhilai, Chhattisgarh, with levels exceeding control areas by 30 times.[15,16] Similarly, communities residing near coal-fired power plants exhibit higher hair mercury levels compared to urban populations without such facilities.[17] While ground observations provide valuable insights into specific regions, chemical transport model simulations offer a powerful tool for comprehensively mapping the spatial and temporal distribution of mercury concentrations and deposition over vast geographical regions. However, existing models vary considerably in their general formulation, spatial resolution, and parameterization of physical and chemical processes. Evaluations from previous studies across different regions[18–20] demonstrate the applicability of these models for regional and global assessments over extended periods. The GEOS-Chem model, in particular, has been successfully applied to analyze the seasonal and spatial patterns of wet mercury deposition in the USA, China, and Europe.[21–25] While extensively validated for various other regions,[26–28] to our knowledge, model-based studies focused on the Indian subcontinent remain scarce. This research aims to address this gap by employing the GEOS-Chem model to investigate the spatiotemporal variability of mercury over India.

This study investigates the spatiotemporal variability of mercury (Hg) over the Indian subcontinent from 2013 to 2017 using the GEOS-Chem (GC) global chemical transport model. The model simulations are validated against observations from ground-based Global Mercury Observation System (GMOS) stations. We employ a suite of widely used global anthropogenic emission inventories (AMAP/UNEP-2010, WHET (2010), EDGAR (2012), STREETS (2013–2015), and AMAP/UNEP-2015) to examine their impact on simulated spatial variations in Hg concentration and deposition. The objectives of this study are to (i) analyze the spatial distribution of Hg arising from these different emission inventories, (ii) evaluate the seasonal variations in wet and dry deposition fluxes and their connection to meteorological parameters and (iii) quantify the contribution of Indian anthropogenic emissions to Hg pollution over the region.

Section 2 details the GEOS-Chem model setup, emission inventories employed, and the characteristics of the GMOS stations used for model evaluation. In Section 3.1, we compare simulated results with measured data from these GMOS sites to assess model performance. Section 3.2 presents the spatial distribution of modeled Hg concentration across the study region. Building upon the validated model, Section 3.3 explores the spatial and temporal variations of Hg wet deposition fluxes, along with the key factors influencing these patterns. Similarly, Section 3.4 delves into the variations and driving forces behind dry deposition fluxes, while Section 3.5 discusses the impacts of Indian anthropogenic emissions on these deposition fluxes. Finally, Section 4 summarizes the key findings of this study and discusses their broader implications.

2 Data and methodology

2.1 Model set-up and simulations

This study employs the GEOS-Chem model[29] (**https://geoschem.github.io/**), version 12.5.0. Global Hg simulations were conducted for the period 2010–2017 at a horizontal resolution of 2° × 2.5°, with the first three years designated as a spin-up period. The simulations were conducted for the widely used global Hg emission inventories, which will be discussed in detail in the next section. Nested simulations were performed over the Asian region (11°S–55°N, 60°E–150°E) at a higher horizontal resolution of 0.5° × 0.625° and 47 vertical layers (surface to 0.01 hPa), maintaining the same vertical resolution as the global model. These simulations covered the period 2013–2017 and employed a six-month spin-up period. Boundary conditions, obtained every three hours from the global simulations, were used for the nested model. Both global and nested simulations used assimilated meteorological data from Modern-Era Retrospective analysis for Research and Applications (MERRA-2).[30] Redox chemistry followed the two step oxidation scheme of Horowitz *et al.* (2017),[31] which considers bromine (Br) as the primary Hg^0 oxidant. Monthly mean Br concentrations were obtained from Schmidt *et al.* (2016).[32] The partitioning of reactive gaseous mercury (RGM) and particulate-bound mercury (PBM) followed the approach of Amos *et al.* (2012).[33] In-cloud photoreduction of Hg^{II} was parameterized based on organic aerosols and NO_2 photolysis abundance. The model also considers emissions from snow and re-emissions of deposited Hg, based on Selin *et al.* (2008).[34]

2.2 Emission inventory

This study utilizes five global emission inventories for Hg: AMAP/UNEP-2010, WHET (2010), EDGARv4.tox2 (2012), STREETS (2013–2015), and AMAP/UNEP-2015. Detailed descriptions of these inventories can be found in the literature.[8,9,25,35,36] Apart from STREETS, the latest available emission from each inventory was applied consistently throughout the simulation period, regardless of their nominal reference year, due to the unavailability of temporal variation in emissions for the other inventories. The STREETS inventory, which varies temporally, provided data from 2000 to 2015, after which it was held constant for the years 2016 and 2017.

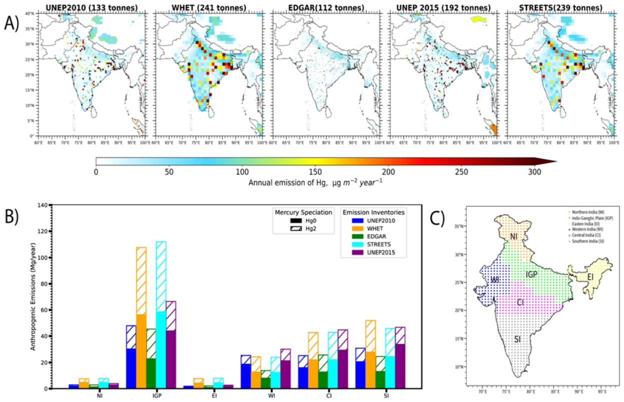

Fig. 1 (A) Spatial distribution of annual anthropogenic Hg emissions (tonnes) across India based on different emission inventories. The inventory name and total Hg emissions (tonnes) for India are included within parentheses in the corresponding map title. (B) Comparison of total anthropogenic Hg emissions (tonnes) across various Indian regions for each emission inventory. (C) The spatial distribution of GEOS-Chem grid points (0.5° × 0.625° resolution) over the Indian subcontinent represented using distinct colors to differentiate the various regions.[37]

Fig. 1A shows the spatial distribution of total anthropogenic Hg emission fluxes from various emission inventories. These inventories differ in their spatial resolution and estimated Hg emissions over India. Notably, WHET and STREETS exhibit similar Hg emissions and spatial resolution (1° × 1°), while EDGAR has the finest resolution (0.1° × 0.1°) but the lowest estimated emissions. A key difference lies in the markedly lower EDGAR estimate for Hg emissions over India from non-ferrous metal production compared to UNEP2010. Total emissions across all these inventories for India fall within the uncertainty range of 104 to 395 Mg A^{-1} according to the recent AMAP/UNEP 2018 report.[9] We conducted global and nested Asian simulations for each emission inventory, along with a sensitivity simulation excluding Indian anthropogenic emissions. Additionally, India was divided into six regions as shown in Fig. 1C (Northern India (NI), Indo-Gangetic Plain (IGP), Central India (CI), Eastern India (EI), Western India (WI), and Southern India (SI)) based on geographical and meteorological conditions[37] to better understand the regional variability of mercury emissions, concentrations and deposition over India.

Fig. 1B illustrates the total anthropogenic Hg emissions across various Indian regions based on the emission inventory. Coal combustion is the dominant contributor, accounting for 53%, 61.8%, and 66.8% of total emissions in AMAP/UNEP 2010, AMAP/UNEP 2015, and EDGAR (2012), respectively. Anthropogenic Hg emissions are highest in the Indo-Gangetic Plain and lowest in Northern and Eastern India. These inventories use population distribution as proxy data to geo-distribute emissions like residential and industrial combustion and for the solid waste incineration sector.[5] Hg(II) and Hg(P) emissions are merged to form the Hg(II) tracer in the GC nested and global models. The Hg(0) : Hg(II) speciation profile varies across inventories: WHET and STREETS share a 53 : 47 ratio, while EDGAR employs 52 : 48. AMAP 2010 and 2015 use 66 : 34 and 68 : 32 ratios for India, respectively.

While India lacks significant geogenic Hg emissions, other sources were considered, including open fire biomass burning (2.11 Mg A^{-1}; Global Fire Emission Database version 2, assuming a Hg/CO emission ratio of 100 nmol mol^{-1}),[38] and emissions from soil (28.25 Mg A^{-1}) were considered. Emissions from snow (0.043 Mg A^{-1}) and land reemissions (3.96 Mg A^{-1}) are very low compared to other emission sources. These re-emissions depend on meteorology and exhibit minimal variation (less than 20%) across the five-year study period. Notably, these re-emission sources are projected to increase with rising anthropogenic emissions.

2.3 Mercury observation data

For this study, we utilized data from Global Mercury Observing System (GMOS) ground-based stations. GMOS is a global Hg monitoring network that provides observations from 35 ground-based monitoring stations in the Northern and Southern Hemispheres, ad hoc cruise campaigns over oceans and seas, and tropospheric studies (GMOS, https://www.gmos.eu). Ground-based stations within the GMOS network utilize Tekran continuous mercury vapor analyzers, except for the

Listvyanka site (LIS), Russia, which employs a Lumex RA-915+ mercury analyzer.[39] GMOS ensures data quality through standardized operating procedures and robust QA/QC protocols.[40]

The limited availability of monitoring data in India (only one station at Kodaikanal, 10.23°N, 77.47°E) severely restricts our ability to capture the spatial variability of mercury concentrations across the vast and diverse Indian landscape. This lack of comprehensive observational data hinders our understanding of the complex interplay between local emission sources, meteorological conditions, and long-range transport of atmospheric mercury over India. To partially address this gap, we incorporated data from six GMOS stations within the nested Asian domain to improve model evaluation. These stations include Everest-K2 (27.96°N, 86.81°E), Mt. Aliao (24.54°N, 101.03°E), Mt. Waliguan (36.29°N, 100.9°E), Mt. Changbai (42.4°N, 128.11°E), Listvyanka (51.85°N, 104.89°E), and Minamata (32.23°N, 130.41°E) (refer to ESI Fig. S1†). In addition to GMOS observations, we incorporated Hg concentration data from various research articles (see ESI Table S1†) for the nested Asian domain.

3 Results

3.1 Model evaluation

To evaluate the performance of our model in simulating daily mercury concentrations, a Taylor diagram (Fig. 2) was employed for data from GMOS monitoring stations.[41] We interpreted the GMOS data primarily as gaseous elemental mercury (GEM, Hg^0) concentration due to minimal proportions of reactive gaseous mercury (RGM) at these sites (less than 2%).[42] The Taylor diagram summarizes key evaluation statistics: correlation coefficient, normalized standard deviation (SD), and normalized centered root mean square error (CRMSE). Both the SD and RMSE are normalized by the standard deviation of the corresponding observed data.

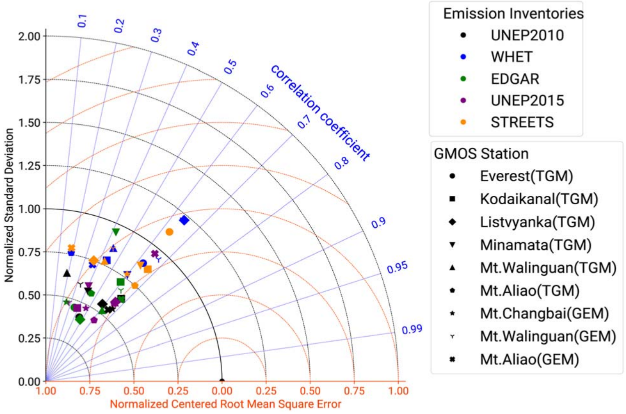

Fig. 2 Comparison of modeled and observed Hg concentrations at GMOS stations. This Taylor diagram summarizes the performance of the model in simulating Hg concentrations at ground-based monitoring stations (GMOS). Each point represents a station, with the distance from the origin reflecting the Root Mean Square Difference (RMSD) between the modeled and observed values. The angle from the horizontal axis corresponds to the correlation coefficient (r), and the distance along the x-axis represents the normalized standard deviation (SD) of the modeled data.

The temporal correlation coefficient (r) between modeled and observed Hg concentrations at GMOS stations exhibited good correlation (>0.6) for most stations (Kodaikanal, Listvyanka, Minamata, Mt. Aliao and Mt. Changbai). Moderate correlation ($0.4 < r < 0.6$) was observed for Everest and Mt. Waliguan. These variations in correlation might be attributed to the complex terrain (higher elevation and hilly terrain) surrounding these stations. The relative bias for both TGM and GEM concentrations at all GMOS stations remained within an acceptable range (±20%).

A detailed analysis of different emission inventories revealed variations in model performance across the GMOS stations. EDGAR performed better at Everest and Mt. Aliao, while WHET excelled at Kodaikanal, Minamata, and Mt. Aliao. Conversely, UNEP2015 demonstrated better agreement with the observations at Listvyanka, Mt. Waliguan, and Mt. Changbai. Further, simulation results were compared with literature data covering regions other than GMOS stations. Simulations using the UNEP2015 emission inventory resulted in a very low mean absolute percentage error (14%) at remote/rural stations like Bayinbuluk, Changdao, and Miyun. At urban sites like Beijing and Shanghai, simulations with WHET and STREETS exhibited a low mean absolute percentage error (17.2%). Given the limited availability of consistent reactive gaseous mercury (RGM) and particulate-bound mercury (PBM) data at most GMOS sites and higher biases in reactive mercury measurements,[43,44] we have excluded these data from our evaluation in Fig. 2 and have averaged the available RGM and PBM data over the measurement period and compared the resulting averages against our model simulations. The model overestimated the concentrations of RGM and PBM compared to the observations at these locations. The magnitude of this overestimation varied depending on the chosen emission inventory. Simulations using UNEP 2015, EDGAR, and UNEP 2010 inventories overestimated these concentrations by a factor of 2, while WHET and STREETS overestimated them by a factor of 4. This can be due to measurement uncertainties associated with losses due to oxidant interference and incomplete capture of RGM.[42,45,46] Additionally, potential inaccuracies in the speciation of Hg in emission inventories might contribute to the overestimation.[33,47,48]

To assess the impact of resolution on Hg concentration, we compared global and nested simulations. Nested simulations exhibited a lower but comparable root mean square error (0.861 ng m^{-3} *vs.* 0.835 ng m^{-3} for global and nested simulations, respectively) and mean absolute percentage error (19.8% *vs.* 19.0% for global and nested simulations, respectively) in concentration compared to the global simulation. Therefore, we employed nested model simulations from different emission inventories to understand spatial and temporal variation over India.

3.2 Surface Hg concentrations

Fig. 3 presents the modeled annual average surface concentrations of total gaseous mercury (TGM), reactive gaseous mercury (RGM), and particulate bound mercury (PBM) across India

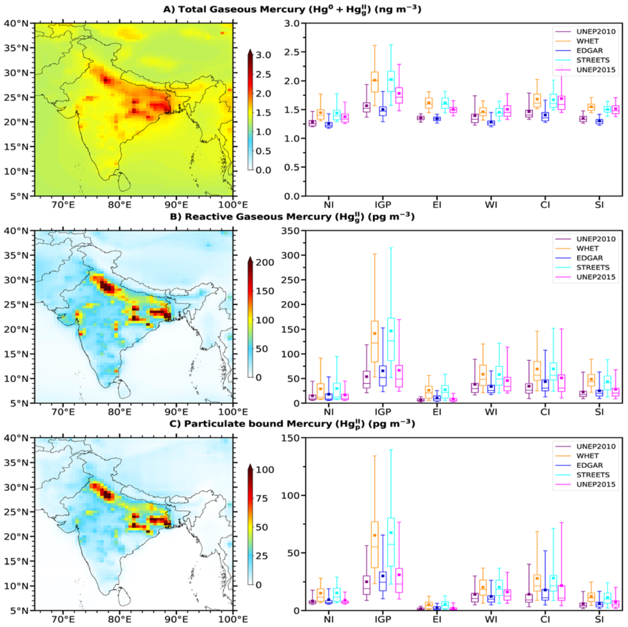

Fig. 3 Spatial distribution of annual average surface concentrations (left panel) from different emission inventories during 2013–2017. Box and whisker plots (right panel) illustrate annual surface concentrations over different regions of India based on the emission inventories used. (A) Total gaseous mercury (TGM, Hg^0 + Hg^{II}_g), (B) reactive gaseous mercury (RGM, Hg^{II}_g), and (C) particulate-bound mercury (PBM, Hg^{II}_p).

during the period 2013–2017. To better understand the spatial variability of mercury concentrations and deposition across India, the results were presented for six regions: Northern India, Indo-Gangetic Plain, Central India, Eastern India, Western India, and Southern India. These regions were defined based on geographical and meteorological conditions[37] rather than population and economic factors. The simulated annual average TGM concentration (1.34–1.64 ng m^{-3}) falls within the typical background range for the northern hemisphere (1.3–1.6 ng m^{-3}).[39] Notably, the simulated TGM concentration at Kodaikanal (only station within India) (1.19–1.43 ng m^{-3}) is lower than the observed annual mean (1.52 ng m^{-3}). As expected, these concentrations exhibit a positive correlation with emissions in the employed inventories.

Fig. 3 (right panel) shows box and whisker plots for Hg concentrations across different Indian regions and emission inventories. Annual mean TGM concentrations are highest over the Indo-Gangetic Plain (1.51–2.02 ng m^{-3}), with the 25th percentile ranging between 1.39 and 1.81 ng m^{-3} and the 75th percentile between 1.57 and 2.17 ng m^{-3}. This region also exhibits the highest emissions. Lower annual mean TGM concentrations (1.26–1.45 ng m^{-3}) are observed in Northern India. These spatial patterns closely mirror the distribution of anthropogenic emissions. The mean and median TGM values across all regions are nearly identical, except in Central India, where the mean is slightly higher due to elevated anthropogenic emissions.

Spatial variations in Reactive Gaseous Mercury (RGM) and Particulate Bound Mercury (PBM) concentrations were also analyzed. RGM concentrations were highest over the Indo-Gangetic Plain (65–147 pg m^{-3}). Conversely, the lowest RGM concentrations were observed in North India (7–27 pg m^{-3}). A similar pattern emerged for PBM, with the highest concentrations (25–67 pg m^{-3}) found over the Indo-Gangetic Plain and the lowest (1.6–5.5 pg m^{-3}) in East India. Notably, the mean values of both RGM and PBM exceed the median across all Indian regions. This suggests a skewed distribution with a few areas having exceptionally higher concentrations. Additionally, RGM and PBM exhibit stronger spatial variability compared to TGM due to their shorter atmospheric lifetimes. There is significant variability in RGM and PBM concentrations across the emission inventories. The higher Hg(II) emissions in the EDGAR inventory compared to UNEP2010 contribute to its consistently higher mean RGM and PBM across most Indian regions (except Western India), as shown in Fig. 3.

3.3 Wet deposition

Wet deposition of Hg(II) includes processes such as rainout and washout resulting from both large-scale and convective precipitation, as well as scavenging processes within convective updrafts.[49] Particle phase Hg(II) is effectively scavenged in the form of a water-soluble aerosol, while gaseous Hg(II) is removed as a highly water-soluble gas.[34] The spatial distribution of the wet deposition flux is determined by anthropogenic emissions, Hg(II) concentration, and precipitation patterns.[21] The spatial distribution of the annual average wet deposition flux (left panel) of Hg over India for 2013–2017 is shown in Fig. 4. The annual average wet deposition of mercury over India (5.37–7.07 μg m^{-2} year^{-1}) exceeds the average value for the northern hemisphere (2.9 μg m^{-2} year^{-1}).[50] Notably, the EDGAR inventory exhibits a higher annual average wet deposition flux compared to UNEP2010. This might be linked to the observed elevation in mean RGM and PBM concentrations from EDGAR in these regions (except Western India), suggesting a potential influence of RGM and PBM levels on wet deposition patterns. Higher wet deposition is observed over Eastern India, the Himalayas, and the windward side of the Western Ghats, reflecting the influence of regional precipitation patterns. This is particularly concerning, given the fragile ecosystems and extensive rice cultivation in these areas. Mercury pollution in rivers, lakes, and rice fields can be exacerbated by atmospheric

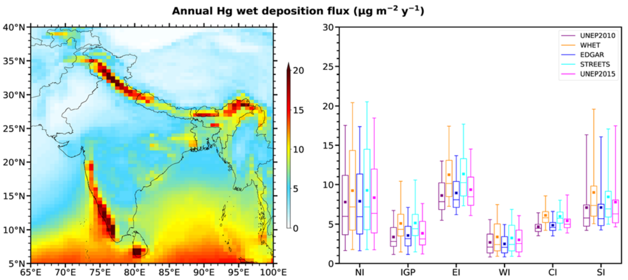

Fig. 4 Spatial distribution of annual average wet deposition flux (left panel) from different emission inventories during 2013–2017. Box and whisker plots (right panel) for different regions of India for the emission inventories used.

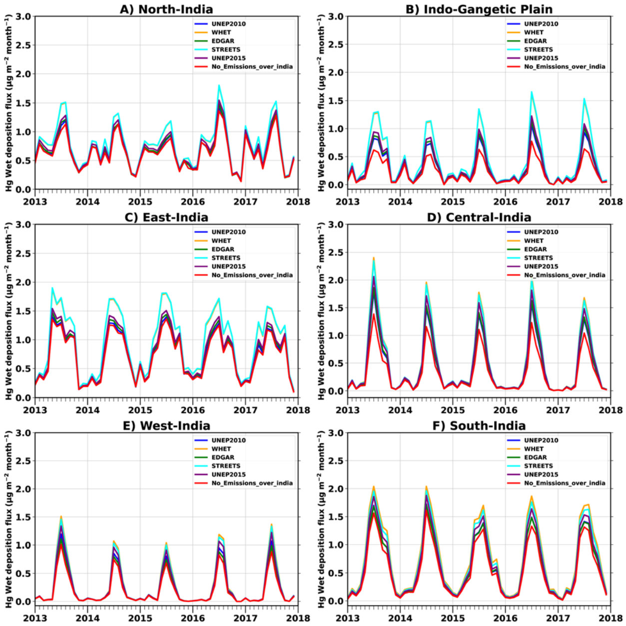

Fig. 5 Monthly mean variation in Hg wet deposition fluxes (μg m^{-2} $month^{-1}$) during 2013–2017 for (A) North India, (B) Indo Gangetic Plain, (C) East India, (D) Central India, (E) West India, and (F) South India, respectively.

deposition in these regions. For example, the Honnamana Kere Lake in the Western Ghats has been identified as a hotspot for mercury pollution due to atmospheric deposition.[51] Newly deposited mercury is more susceptible to methylation in rice-planting areas, potentially leading to elevated mercury levels in rice grains.[52,53]

The climate over India, as classified by the Indian Meteorological Department (IMD), consists of four distinct seasons: winter (January–February), summer (March–May), monsoon (June–September), and post-monsoon (October–December) (**https://www.imdpune.gov.in/Reports/glossary.pdf**). The monsoon season is crucial, receiving a staggering 60–90% of annual rainfall over India.[54] Summer brings intense heat waves and droughts, while winter experiences lower temperatures, dry atmospheric conditions, and minimal precipitation. The post-monsoon season witnesses a shift in the wind direction from southwesterly to northeasterly, accompanied by low relative humidity over Northern and Western India.[55] Thus, it is important to study the monthly variation of mercury deposition over the Indian region.

Fig. 5 illustrates the monthly variations in modeled wet deposition fluxes (μg m^{-2} $month^{-1}$) across Indian regions for different emission inventories, including a simulation with Indian emissions turned off. Notably, the monsoon season contributes a substantial 67% of the total annual wet deposition flux over India. Except for Northern India, all regions experience higher wet deposition during the monsoon compared to the combined deposition of the remaining seasons. Mercury wet deposition during the monsoon season is reduced by 24% compared to an average reduction of 17.8% across all seasons when Indian emissions are excluded. Summer exhibits the highest wet deposition over Northern and Eastern India. This phenomenon might be attributed to westerly winds, a key synoptic system transporting rain and snow eastward across the Himalayas during winter and summer.[56] These winds may also facilitate the long-distance transport of Hg(II) from Central Asia to the Himalayas.[57] The post-monsoon season witnesses the highest wet deposition in Southern India, likely due to the influence of northeasterly monsoon winds.

A strong correlation ($R > 0.75$) exists between annual precipitation and total wet deposition flux across all regions except Northern India ($R = 0.70$). This indicates that precipitation is a key driver of Hg wet deposition, explaining 56–60% of the total variance (R^2) in Hg wet deposition across the country. Since the GEOS-Chem model relies on MERRA-2 meteorological data, we evaluated its performance by comparing modeled monthly precipitation with observed rainfall data from the India Meteorological Department (IMD) gridded rainfall datasets[58] and the GPM IMERG satellite product[59] (see ESI Fig. S6†). The correlation coefficient between MERRA-2 precipitation and IMD data for India is 0.69, while the correlation between MERRA-2 and IMERG data is 0.74. This indicates a good performance of MERRA-2 over India, although complex terrain might pose challenges in resolving orographic effects.[60] While MERRA2 overestimates precipitation in Northern and Eastern India, the observed percent change in model precipitation between years (25% from 2013 to 2014 in Northern India and 16.5% from 2014 to 2015 in Eastern India) and the corresponding 5% variation in annual wet deposition fluxes suggest that this has a limited impact on our overall results. Despite higher deposition fluxes, studies over the Himalayas have demonstrated that mercury concentrations in wet deposition are lower during the monsoon season compared to non-monsoon seasons. This reduced concentration is likely attributed to a dilution effect, which can counteract the increased Hg loading from atmospheric deposition.[61–63]

Precipitation types also play a significant role in wet deposition. The GC model distinguishes between large-scale wet deposition (LS), caused by large-scale and anvil precipitation, and convective wet deposition (Conv), driven by convective rainfall. Notably, large-scale wet deposition contributes a higher share (79–82%) to the total deposition compared to convective wet deposition (18–21%) across India. However, convective wet deposition becomes particularly significant over the Indo-Gangetic Plain, especially during the summer season (March–May). Interestingly, the correlation coefficient (R) between convective wet deposition and convective precipitation is lower in Eastern India ($R = 0.50$–0.53) compared to other regions ($R > 0.78$). In contrast, large-scale wet deposition exhibits a strong correlation with total deposition across Eastern India ($R > 0.77$). Indian anthropogenic emissions contribute a larger fraction (30.5%) to convective wet deposition compared to large-scale wet deposition (19.8%).

3.4 Dry deposition

Dry deposition of Hg plays a critical role compared to wet deposition for terrestrial ecosystems.[64] Dry deposition accounts for 72–74% of total (both wet and dry) deposition flux over the Indian region. However, wet deposition becomes significant during the monsoon season. These ecosystems function as storage basins for atmospheric Hg, efficiently retaining deposited mercury in vegetation and soils.[65,66] A portion of the deposited mercury re-enters the atmosphere, enters watersheds or soils, and ultimately becomes a source for rivers and marine sediments.[67] Terrestrial ecosystems can act as both sources and sinks of atmospheric Hg, depending on environmental conditions.[68,69] The dry deposition flux is typically calculated as the product of atmospheric Hg concentration and dry deposition velocity.[70] In GEOS-Chem, similar to many chemical transport models (CTMs), the dry deposition velocity for Gaseous Elemental Mercury (GEM) and Reactive Gaseous Mercury (RGM) employs a series-resistance scheme[71] with updates to account for the effect of the Leaf Area Index (LAI) on stomatal resistivity,[72] while Particulate Bound Mercury (PBM) utilizes an aerosol deposition scheme.[73,74] The Leaf Area Index (LAI) is a dimensionless measure representing the total one-sided green leaf area of a plant canopy per unit of ground area.[75] It is a crucial parameter in Chemical Transport Models (CTMs) for estimating dry deposition, helping to accurately quantify the vegetation surface area and capture seasonal variations in land cover by representing fractional vegetation cover and density.[76]

Fig. 6 (left panel) depicts the spatial distribution of annual average dry deposition fluxes for different emission inventories during 2013–2017. The highest Hg^0 dry deposition occurs in Eastern India (14.1–16.6 μg m^{-2} $year^{-1}$), while the lowest is observed in Northern India (5.2–6.0 μg m^{-2} $year^{-1}$). Dry deposition of Hg^0 flux accounts for about 64–75% of the total annual dry deposition of all mercury species. Hg^0 dry deposition is highest in Eastern India (14.1–16.6 μg m^{-2} $year^{-1}$) and lowest in Northern India (5.2–6.0 μg m^{-2} $year^{-1}$). A significant positive correlation (correlation coefficient: 0.82–0.90) exists between dry deposition velocity and Hg^0 dry deposition. Dry deposition of reactive gaseous mercury (Hg^{II}_g, RGM) contributes 23–34% to the total annual dry deposition. RGM dry deposition is highest in the Indo-Gangetic Plain (4.3–11.1 μg m^{-2} $year^{-1}$) and lowest in Northern India (1.7–2.7 μg m^{-2} $year^{-1}$). Notably, RGM dry deposition patterns are more strongly linked to concentration patterns (correlation coefficient: 0.51–0.62) than dry depositional velocity (0.13–0.23). Particulate bound mercury (Hg^{II}_p, PBM) dry deposition contributes only about 1–2% to the total annual dry deposition. PBM dry deposition exhibits a similar spatial distribution to RGM, with the highest fluxes (0.25–0.66 μg m^{-2} $year^{-1}$) in the Indo-Gangetic Plain and the lowest (0.07–0.11 μg m^{-2} $year^{-1}$) in Northern India. Similar to RGM, PBM dry deposition is more closely associated with concentration patterns (correlation coefficient: 0.54–0.60) than dry depositional velocity (almost zero).

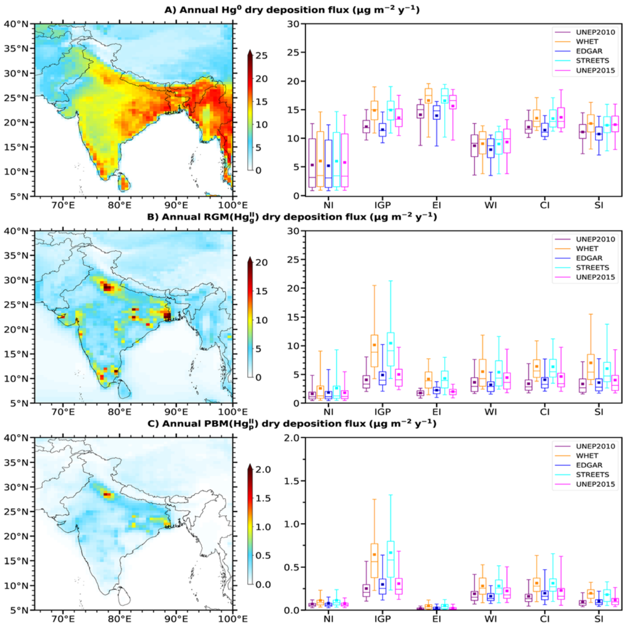

Fig. 6 Spatial distribution of annual average dry deposition flux (left panel) from different emission inventories during 2013–2017. Box and whisker plots (right panel) illustrate dry deposition fluxes over different regions of India based on the emission inventories used. (A) GEM (gaseous elemental mercury, Hg^0), (B) RGM (reactive gaseous mercury, Hg^{II}_g), and (C) PBM (particulate-bound mercury, Hg^{II}_p).

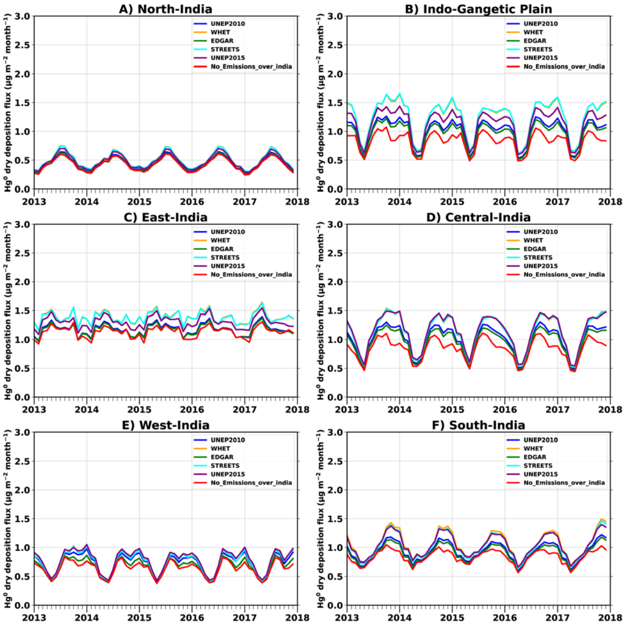

Fig. 7 Monthly mean variation in Hg^0 dry deposition fluxes (μg m^{-2} $month^{-1}$) during 2013–2017 for (A) North India, (B) Indo Gangetic Plain, (C) East India, (D) Central India, (E) West India, and (F) South India, respectively.

Fig. 7 depicts the monthly variation in modeled Hg^0 dry deposition fluxes (μg m^{-2} $month^{-1}$) across Indian regions for different emission inventories and with a sensitivity simulation excluding Indian anthropogenic emissions. GEM dry deposition peaks at the end of the monsoon (August–September) and persists through the post-monsoon season across all regions. A strong positive correlation (correlation coefficient > 0.7) exists between the leaf area index (LAI) and GEM dry deposition, suggesting that LAI variations (ESI Fig. S11†) significantly influence the observed spatial GEM dry deposition in India. GEM concentrations are lowest during the monsoon season and highest during the post-monsoon season over India. This is consistent with the finding in ref. 67 and 77, where both GEM concentrations and CO_2 concentrations were reported to be lowest during the summer growing (which coincides with the monsoon season in India) season due to enhanced plant growth rate. Further, there is a 13.7% and 24.0% decrease in GEM dry deposition flux due to Indian anthropogenic emissions in monsoon and post-monsoon seasons, respectively. RGM exhibits the highest dry deposition flux during summer and the lowest during the monsoon season (ESI Fig. S10†). Peak post-monsoon dry deposition in the Indo-Gangetic Plain and Western India coincides with higher RGM concentrations during this period. As RGM is more soluble and reactive than GEM, its dry deposition velocity is generally higher.[70] RGM dry deposition velocity is highest during the monsoon season and lowest during winter. The dry deposition velocity of RGM is most dependent on wind speed, and the wind speed is highest over India in May.[78] The RGM concentrations are lowest during the monsoon. In contrast, PBM dry deposition is highest in winter and lowest during the monsoon (ESI Fig. S10†) following the seasonal pattern of PBM concentrations. The model simulates RGM and PBM dry deposition fluxes primarily following concentration variations rather than dry deposition velocity.

3.5 Impact of Indian anthropogenic emissions on deposition

A sensitivity simulation was performed by switching off all Indian anthropogenic emissions to isolate the influence of regional sources on deposition and concentrations. Fig. 8 (left panels) illustrates the annual mean wet and dry deposition fluxes over India attributed to global background sources (natural sources from India and natural + anthropogenic sources outside India) and Indian anthropogenic emissions (middle panels). The model indicates that these external sources contribute to a maximum in wet deposition stretching across Northern and Eastern India, with another peak observed over the Western Ghats. To quantify the impact of Indian anthropogenic emissions, we calculated their contribution by taking the difference between simulations with and without these emissions. Wet deposition fluxes decrease by only 7% around Northern and Eastern India and 11.8% around the Western Ghats, suggesting the influence of global mercury transport in these regions. However, these fluxes decrease substantially in the Indo-Gangetic Plain (37.3%) and Central India (30.2%), highlighting the substantial influence of local emissions.

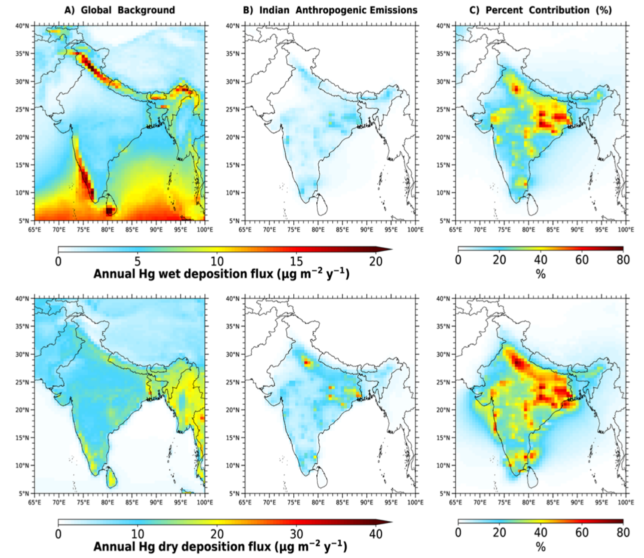

Fig. 8 Contributions of global background and Indian anthropogenic emissions to mercury wet (top panel) and dry deposition (bottom panel) during 2013–2017. (A) Absolute wet and dry deposition fluxes ($\mu g\ m^{-2}\ year^{-1}$) due to global background emissions. (B) Absolute wet and dry deposition fluxes ($\mu g\ m^{-2}\ year^{-1}$) due to Indian anthropogenic emissions. (C) Percentage contribution of Indian anthropogenic emissions to total wet and dry deposition.

Indian anthropogenic emissions account for 33.5% (with the range varying from 26.4% using the UNEP2010 inventory to 42.4% using the STREETS inventory) of the total dry deposition within the region. There is a decrease in GEM dry deposition fluxes across all regions of India due to local anthropogenic emissions, with an average reduction of 18.3% (12.4% using the EDGAR inventory to 22.4% using the STREETS inventory). However, seasonal patterns in GEM dry deposition influenced by meteorological conditions persisted even without local emissions. This decrease is most pronounced in the Indo-Gangetic Plain and Central India, where dry deposition fluxes decreased by 25.2% (17.4–32.3%) and 21.3% (15.5–24.8%). In contrast, the reduction in North India was less severe, with a decrease of only 9.8% (6.4–13.3%). This spatial pattern aligns with the decrease in gaseous elemental mercury (GEM) concentrations (ESI S12†). The highest reduction (25.5% and 21.3%) occurred in the Indo-Gangetic Plain and Central India, respectively, and the lowest (7%) was observed in North India. Indian anthropogenic emissions substantially impacted dry deposition fluxes of both reactive gaseous mercury (RGM) and particulate-bound mercury (PBM), leading to an average decrease of 68.3% (60.1–77.8%) and 75.7% (69.1–83.1%), respectively. Spatially, the Indo-Gangetic Plain experienced the most substantial decrease (76%) in RGM and PBM dry deposition, while the lowest decrease (29%) was observed in Northern India. Similar to the spatial patterns observed for concentration decrease, there is an averaged 80% (74.5–86.3%) reduction in annual average RGM concentrations and an averaged 81% (75.9–86.8%) reduction in PBM concentrations across India, respectively.

4 Conclusion

This study investigated the spatial and seasonal variations of Hg concentration and deposition (dry and wet) across India from 2013 to 2017. We employed the GEOS-Chem model with established global emission inventories (UNEP2010, WHET, EDGAR, STREETS, and UNEP2015). India's Hg emissions are predominantly anthropogenic, with coal combustion as the major source, with minimal contributions from natural sources (biomass burning and geothermal activity). Model results for total gaseous mercury (TGM) concentration were within the acceptable error range (±20%) and effectively captured seasonal variations. However, reactive gaseous mercury (RGM) and particulate-bound mercury (PBM) were overestimated compared to observations, likely due to the measurement uncertainties and potential inaccuracies in emission allocation. Consistent with emission patterns, model results reveal elevated concentrations of TGM, RGM, and PBM along the Indo-Gangetic Plain, reflecting high anthropogenic activity over the region. Hg(II) emissions significantly influence RGM and PBM concentrations, ultimately influencing their wet and dry deposition.

The study also revealed that Hg wet deposition is highest over the Western Ghats and Himalayan foothills due to increased precipitation. Wet deposition exhibited strong seasonality, with peak values occurring during the monsoon season (contributing 67% of the annual wet deposition). Large-scale wet deposition contributed more to the total mercury deposition in India than localized convective wet deposition. Sensitivity analysis further reinforces this, demonstrating a 21.9% reduction (with the range varying from 14.9% using the UNEP2010 inventory to 29.5% using the STREETS inventory) in wet deposition fluxes across India when excluding anthropogenic emissions within the country. This highlights the substantial influence of global mercury transport on mercury fluxes in the Indian region. Dry deposition exceeded wet deposition annually, accounting for 70–75% of the total deposition. Dry Gaseous Elemental Mercury (GEM,Hg^0) deposition, the dominant form (75% of total dry deposition), is highest over Eastern India due to an increased leaf area index (vegetation). Dry deposition exhibited strong seasonality, with peak values during the monsoon and post-monsoon seasons. Furthermore, our analysis highlights the substantial contribution of Indian anthropogenic emissions to total Hg dry deposition fluxes. Excluding these emissions from the model simulation resulted in a 33.5% reduction (with the range varying from 26.4% using the UNEP2010 inventory to 42.4% using the STREETS inventory) in dry deposition across India, underscoring the dominant role of human activities in Hg pollution.

Recent updates to the GEOS-Chem model, such as the updated oxidation chemical mechanism[79] and higher biological reactivity of GEM in the dry deposition scheme,[28] could potentially alter the spatial and temporal distribution of mercury over India. These updates have shown to decrease global mercury wet deposition fluxes while increasing dry deposition fluxes[28] compared to our study. Future studies incorporating these model updates could provide a more refined understanding of mercury pollution dynamics in the region. Additionally, the development of Indian-specific gridded anthropogenic inventories and specific trends for these emissions would be beneficial for enhancing the accuracy of mercury modeling and assessment in India. Moreover, expanding Hg measurement networks across diverse Indian regions is crucial for refining model accuracy.

Data availability

The GEOS-Chem model is an open-source model and can be obtained at **https://doi.org/10.5281/zenodo.3403111**. The model description can be found at Welcome to the GEOS-Chem website (**https://geoschem.github.io**). Hg observations from the GMOS are accessible at **https://sdi.iia.cnr.it/gos4mcat/srv/eng/catalog.search#/home**. IMD rainfall data are available at the Climate Monitoring and Prediction Group (**https://imdpune.gov.in/cmpg/Griddata/Rainfall_25_NetCDF.html**). The GPM IMERG satellite precipitation dataset is available at GES DISC Dataset: GPM IMERG Final Precipitation L3 1 month 0.1° × 0.1° V06 (GPM_3IMERGM06) (**https://disc.gsfc.nasa.gov/datasets/GPM_3IMERGM_06/summary**).

Author contributions

Chakradhar Reddy Malasani: conceptualization, formal analysis, methodology, validation, visualisation, writing – original draft, and writing – review & editing; Basudev Swain: conceptualization, methodology, formal analysis, and writing – review & editing; Ankit Patel: formal analysis and writing – review & editing; Yaswanth Pulipati: formal analysis and writing – review & editing; Nidhi L. Anchan: formal analysis; Amit Sharma: writing – review & editing; Marco Vountas: writing – review & editing; Pengfei Liu: methodology and writing – review & editing; Sachin S. Gunthe: conceptualization, formal analysis, methodology, supervision, and writing – review & editing.

Conflicts of interest

The authors declare no conflicts of interest relevant to this study.

Acknowledgements

Authors like to acknowledge all the researchers and technicians from the GMOS network (**https://sdi.iia.cnr.it/gos4mcat/srv/eng/catalog.search#/home**) for providing the observed mercury measured data used in this study. The use of the high-performance computer Raven (**https://www.mpcdf.mpg.de/services/supercomputing/raven**) is acknowledged. This work has been partly funded by the Deutsche Forschungsgemeinschaft (DFG, German Research Foundation) within the project "Arctic Amplification: Climate Relevant Atmospheric and Surface Processes, and Feedback Mechanisms (AC)^3" as Transregional Collaborative Research Center (TRR) 172, Project-ID 268020496. Ankit Patel acknowledges the financial support from DST-INSPIRE Fellowship, Project No. 2020/IF200113/SP23241491CE. Authors are grateful to two anonymous reviewers for their valuable inputs and suggestions during the review process.

References

1 D. Mergler, H. A. Anderson, L. H. M. Chan, K. R. Mahaffey, M. Murray, M. Sakamoto and A. H. Stern, *Ambio*, 2007, **36**, 3–11.
2 A. M. Scheuhammer, M. W. Meyer, M. B. Sandheinrich and M. W. Murray, *Ambio*, 2007, **36**, 12–19.

3 N. Pirrone, S. Cinnirella, X. Feng, R. B. Finkelman, H. R. Friedli, J. Leaner, R. Mason, A. B. Mukherjee, G. B. Stracher, D. G. Streets and K. Telmer, *Atmos. Chem. Phys.*, 2010, **10**, 5951–5964.

4 R. P. Mason, *Mercury Fate and Transport in the Global Atmosphere*, Springer US, 2009, pp. 173–191.

5 E. Pacyna, J. Pacyna, K. Sundseth, J. Munthe, K. Kindbom, S. Wilson, F. Steenhuisen and P. Maxson, *Atmos. Environ.*, 2010, **44**, 2487–2499.

6 W. H. Schroeder and J. Munthe, *Atmos. Environ.*, 1998, **32**, 809–822.

7 S. Lindberg, R. Bullock, R. Ebinghaus, D. Engstrom, X. Feng, W. Fitzgerald, N. Pirrone, E. Prestbo and C. Seigneur, *Ambio*, 2007, **36**, 19–33.

8 A. Monitoring, *Arctic Monitoring and Assessment Programme*, 2013.

9 A. Monitoring, *Technical background report for the global mercury assessment*, 2018.

10 L. Burger Chakraborty, A. Qureshi, C. Vadenbo and S. Hellweg, *Environ. Sci. Technol.*, 2013, **47**, 8105–8113.

11 P. Rafaj, I. Bertok, J. Cofala and W. Schoepp, *Atmos. Environ.*, 2013, **79**, 472–479.

12 B. M. Sharma, G. K. Bharat, K. Šebková and M. Scheringer, *Environ. Sci. Eur.*, 2019, **31**, 1–12.

13 H. Lin, Y. Tong, X. Yin, Q. Zhang, H. Zhang, H. Zhang, L. Chen, S. Kang, W. Zhang, J. Schauer, B. de Foy, X. Bu and X. Wang, *Atmos. Chem. Phys.*, 2019, **19**, 1373–1391.

14 H. Lin, Y. Tong, C. Yu, L. Chen, X. Yin, Q. Zhang, S. Kang, L. Luo, J. Schauer, B. de Foy and X. Wang, *Atmos. Chem. Phys.*, 2022, **22**, 2651–2668.

15 S. Pervez, A. Koshle and Y. Pervez, *Atmos. Chem. Phys.*, 2010, **10**, 5535–5549.

16 R. Sharma and S. Pervez, *Environ. Geochem. Health*, 2005, **27**, 39–45.

17 K. L. Subhavana, A. Qureshi and A. Roy, *J. Exposure Sci. Environ. Epidemiol.*, 2019, **29**, 697–705.

18 J. Bieser, V. Matthias, O. Travnikov, I. M. Hedgecock, C. Gencarelli, F. D. Simone, A. Weigelt and J. Zhu, *Springer Proceedings in Complexity*, Springer International Publishing, 2016, pp. 519–523.

19 O. R. Bullock Jr, D. Atkinson, T. Braverman, K. Civerolo, A. Dastoor, D. Davignon, J.-Y. Ku, K. Lohman, T. C. Myers and R. J. Park, *J. Geophys. Res.: Atmos.*, 2008, **113**, D17310.

20 O. Travnikov, H. Angot, P. Artaxo, M. Bencardino, J. Bieser, F. D'Amore, A. Dastoor, F. D. Simone, M. del Carmen Diéguez, A. Dommergue, R. Ebinghaus, X. B. Feng, C. N. Gencarelli, I. M. Hedgecock, O. Magand, L. Martin, V. Matthias, N. Mashyanov, N. Pirrone, R. Ramachandran, K. A. Read, A. Ryjkov, N. E. Selin, F. Sena, S. Song, F. Sprovieri, D. Wip, I. Wängberg and X. Yang, *Atmos. Chem. Phys.*, 2017, **17**, 5271–5295.

21 Y. Zhang, L. Jaeglé, A. van Donkelaar, R. V. Martin, C. D. Holmes, H. M. Amos, Q. Wang, R. Talbot, R. Artz, S. Brooks, W. Luke, T. M. Holsen, D. Felton, E. K. Miller, K. D. Perry, D. Schmeltz, A. Steffen, R. Tordon, P. Weiss-Penzias and R. Zsolway, *Atmos. Chem. Phys.*, 2012, **12**, 6095–6111.

22 E. S. Corbitt, D. J. Jacob, C. D. Holmes, D. G. Streets and E. M. Sunderland, *Environ. Sci. Technol.*, 2011, **45**, 10477–10484.

23 L. Chen, H. H. Wang, J. F. Liu, Y. D. Tong, L. B. Ou, W. Zhang, D. Hu, C. Chen and X. J. Wang, *Atmos. Chem. Phys.*, 2014, **14**, 10163–10176.

24 S. Song, N. E. Selin, A. L. Soerensen, H. Angot, R. Artz, S. Brooks, E.-G. Brunke, G. Conley, A. Dommergue, R. Ebinghaus, T. M. Holsen, D. A. Jaffe, S. Kang, P. Kelley, W. T. Luke, O. Magand, K. Marumoto, K. A. Pfaffhuber, X. Ren, G.-R. Sheu, F. Slemr, T. Warneke, A. Weigelt, P. Weiss-Penzias, D. C. Wip and Q. Zhang, *Atmos. Chem. Phys.*, 2015, **15**, 7103–7125.

25 Y. Zhang, D. J. Jacob, H. M. Horowitz, L. Chen, H. M. Amos, D. P. Krabbenhoft, F. Slemr, V. L. S. Louis and E. M. Sunderland, *Proc. Natl. Acad. Sci. U. S. A.*, 2016, **113**, 526–531.

26 S. MacFarlane, J. A. Fisher, H. M. Horowitz and V. Shah, *Environ. Sci.: Processes Impacts*, 2022, **24**, 1474–1493.

27 F. Yue, Z. Xie, Y. Zhang, J. Yan and S. Zhao, *Environ. Sci. Technol.*, 2022, **56**, 2968–2976.

28 A. Feinberg, T. Dlamini, M. Jiskra, V. Shah and N. E. Selin, *Environ. Sci.: Processes Impacts*, 2022, **24**, 1303–1318.

29 I. Bey, D. J. Jacob, R. M. Yantosca, J. A. Logan, B. D. Field, A. M. Fiore, Q. Li, H. Y. Liu, L. J. Mickley and M. G. Schultz, *J. Geophys. Res.: Atmos.*, 2001, **106**, 23073–23095.

30 R. Gelaro, W. McCarty, M. J. Suárez, R. Todling, A. Molod, L. Takacs, C. A. Randles, A. Darmenov, M. G. Bosilovich, R. Reichle, K. Wargan, L. Coy, R. Cullather, C. Draper, S. Akella, V. Buchard, A. Conaty, A. M. da Silva, W. Gu, G.-K. Kim, R. Koster, R. Lucchesi, D. Merkova, J. E. Nielsen, G. Partyka, S. Pawson, W. Putman, M. Rienecker, S. D. Schubert, M. Sienkiewicz and B. Zhao, *J. Clim.*, 2017, **30**, 5419–5454.

31 H. M. Horowitz, D. J. Jacob, Y. Zhang, T. S. Dibble, F. Slemr, H. M. Amos, J. A. Schmidt, E. S. Corbitt, E. A. Marais and E. M. Sunderland, *Atmos. Chem. Phys.*, 2017, **17**, 6353–6371.

32 J. A. Schmidt, D. J. Jacob, H. M. Horowitz, L. Hu, T. Sherwen, M. J. Evans, Q. Liang, R. M. Suleiman, D. E. Oram, M. L. Breton, C. J. Percival, S. Wang, B. Dix and R. Volkamer, *J. Geophys. Res.: Atmos.*, 2016, **121**, 11819–11835.

33 H. M. Amos, D. J. Jacob, C. D. Holmes, J. A. Fisher, Q. Wang, R. M. Yantosca, E. S. Corbitt, E. Galarneau, A. P. Rutter, M. S. Gustin, A. Steffen, J. J. Schauer, J. A. Graydon, V. L. S. Louis, R. W. Talbot, E. S. Edgerton, Y. Zhang and E. M. Sunderland, *Atmos. Chem. Phys.*, 2012, **12**, 591–603.

34 N. E. Selin and D. J. Jacob, *Atmos. Environ.*, 2008, **42**, 5193–5204.

35 M. Muntean, G. Janssens-Maenhout, S. Song, A. Giang, N. E. Selin, H. Zhong, Y. Zhao, J. G. Olivier, D. Guizzardi, M. Crippa, E. Schaaf and F. Dentener, *Atmos. Environ.*, 2018, **184**, 56–68.

36 D. G. Streets, H. M. Horowitz, Z. Lu, L. Levin, C. P. Thackray and E. M. Sunderland, *Atmos. Environ.*, 2019, **201**, 417–427.

37 L. M. David, A. R. Ravishankara, J. K. Kodros, C. Venkataraman, P. Sadavarte, J. R. Pierce, S. Chaliyakunnel and D. B. Millet, *J. Geophys. Res.: Atmos.*, 2018, **123**, 3688–3703.

38 C. D. Holmes, D. J. Jacob, E. S. Corbitt, J. Mao, X. Yang, R. Talbot and F. Slemr, *Atmos. Chem. Phys.*, 2010, **10**, 12037–12057.

39 F. Sprovieri, N. Pirrone, M. Bencardino, F. D'Amore, F. Carbone, S. Cinnirella, V. Mannarino, M. Landis, R. Ebinghaus, A. Weigelt, E.-G. Brunke, C. Labuschagne, L. Martin, J. Munthe, I. Wängberg, P. Artaxo, F. Morais, H. de Melo Jorge Barbosa, J. Brito, W. Cairns, C. Barbante, M. del Carmen Diéguez, P. E. Garcia, A. Dommergue, H. Angot, O. Magand, H. Skov, M. Horvat, J. Kotnik, K. A. Read, L. M. Neves, B. M. Gawlik, F. Sena, N. Mashyanov, V. Obolkin, D. Wip, X. B. Feng, H. Zhang, X. Fu, R. Ramachandran, D. Cossa, J. Knoery, N. Marusczak, M. Nerentorp and C. Norstrom, *Atmos. Chem. Phys.*, 2016, **16**, 11915–11935.

40 F. D'Amore, M. Bencardino, S. Cinnirella, F. Sprovieri and N. Pirrone, *Environ. Sci.: Processes Impacts*, 2015, **17**, 1482–1491.

41 K. E. Taylor, *J. Geophys. Res.: Atmos.*, 2001, **106**, 7183–7192.

42 M. S. Gustin, H. M. Amos, J. Huang, M. B. Miller and K. Heidecorn, *Atmos. Chem. Phys.*, 2015, **15**, 5697–5713.

43 C. D. McClure, D. A. Jaffe and E. S. Edgerto, *Environ. Sci. Technol.*, 2014, **48**, 11437–11444.

44 M. S. Gustin, S. M. Dunham-Cheatham, S. Lyman, M. Horvat, D. A. Gay, J. Gacnik, L. Gratz, G. Kempkes, A. Khalizov and C. J. Lin, *Environ. Sci. Technol.*, 2024, **58**, 12853–12864.

45 S. N. Lyman, D. A. Jaffe and M. S. Gustin, *Atmos. Chem. Phys.*, 2010, **10**, 8197–8204.

46 J. Huang and M. S. Gustin, *Environ. Sci. Technol.*, 2015, **49**, 6102–6108.

47 G. Kos, A. Ryzhkov, A. Dastoor, J. Narayan, A. Steffen, P. A. Ariya and L. Zhang, *Atmos. Chem. Phys.*, 2013, **13**, 4839–4863.

48 J. Bieser, F. De Simone, C. Gencarelli, B. Geyer, I. Hedgecock, V. Matthias, O. Travnikov and A. Weigelt, *Environ. Sci. Pollut. Res.*, 2014, **21**, 9995–10012.

49 H. Liu, D. J. Jacob, I. Bey and R. M. Yantosca, *J. Geophys. Res.: Atmos.*, 2001, **106**, 12109–12128.

50 J. Leiva González, L. A. Diaz-Robles, F. Cereceda-Balic, E. Pino-Cortés and V. Campos, *Atmosphere*, 2022, **13**, 1226.

51 I. A. Mir, J. Jaiswal and A. Bhattacharya, *Research Square*, 2023, preprint, DOI: 10.21203/rs.3.rs-3166330/v1.

52 N. Cherian, V. Arunbabu and M. Mohan, *Environ. Nanotechnol., Monit. Manage.*, 2024, **21**, 100916.

53 L. Wang, J. Han, H. B. Katuwal, P. Xia, X. Xu, X. Feng and G. Qiu, *Ecotoxicol. Environ. Saf.*, 2021, **228**, 113019.

54 R. P. Shukla and B. Huang, *Climate Dynamics*, 2015, **46**, 1977–1990.

55 S. Attri and A. Tyagi, *Climate Profile of India*, Research Center, India Meteorology Department, New Delhi, India, 2010.

56 A. B. Shrestha and R. Aryal, *Regional Environmental Change*, 2010, **11**, 65–77.

57 J. Huang, S. Kang, R. Yin, M. Lin, J. Guo, K. Ram, C. Li, C. Sharma, L. Tripathee, S. Sun and F. Wang, *Environ. Sci. Technol.*, 2020, **54**, 5429–5436.

58 D. Pai, M. Rajeevan, O. Sreejith, B. Mukhopadhyay and N. Satbha, *MAUSAM*, 2014, **65**, 1–18.

59 G. J. Huffman, E. F. Stocker, D. T. Bolvin, E. J. Nelkin and J. Tan, *GPM IMERG Final Precipitation L3 1 Month 0.1 Degree × 0.1 Degree V06*, Goddard Earth Sciences Data and Information Services Center (GES DISC), Greenbelt, MD, 2021, accessed: 15 April 2024.

60 K. Hamal, S. Sharma, N. Khadka, B. Baniya, M. Ali, M. S. Shrestha, T. Xu, D. Shrestha and B. Dawadi, *Hydrology*, 2020, **7**, 40.

61 L. Tripathee, S. Kang, J. Huang, C. M. Sharma, M. Sillanpää, J. Guo and R. Paudyal, *Atmos. Environ.*, 2014, **95**, 231–238.

62 L. Tripathee, J. Guo, S. Kang, R. Paudyal, J. Huang, C. M. Sharma, Q. Zhang, P. Chen, P. S. Ghimire and M. Sigdel, *Sci. Total Environ.*, 2019, **655**, 1207–1217.

63 J. Huang, S. Kang, W. Tang, M. He, J. Guo, Q. Zhang, X. Yin and L. Tripathee, *Sci. Total Environ.*, 2022, **804**, 150124.

64 L. P. Wright, L. Zhang and F. J. Marsik, *Atmos. Chem. Phys.*, 2016, **16**, 13399–13416.

65 X. Faïn, D. Obrist, A. Pierce, C. Barth, M. S. Gustin and D. P. Boyle, *Geochim. Cosmochim. Acta*, 2011, **75**, 2379–2392.

66 H. Hintelmann, R. Harris, A. Heyes, J. P. Hurley, C. A. Kelly, D. P. Krabbenhoft, S. Lindberg, J. W. Rudd, K. J. Scott and V. L. St. Louis, *Environ. Sci. Technol.*, 2002, **36**, 5034–5040.

67 J. Zhou, D. Obrist, A. Dastoor, M. Jiskra and A. Ryjkov, *Nat. Rev. Earth Environ.*, 2021, **2**, 269–284.

68 Y. Agnan, T. L. Dantec, C. W. Moore, G. C. Edwards and D. Obrist, *Environ. Sci. Technol.*, 2015, **50**, 507–524.

69 D. Obrist, E. M. Roy, J. L. Harrison, C. F. Kwong, J. W. Munger, H. Moosmüller, C. D. Romero, S. Sun, J. Zhou and R. Commane, *Proc. Natl. Acad. Sci. U. S. A.*, 2021, **118**, e2105477118.

70 L. Zhang, L. P. Wright and P. Blanchard, *Atmos. Environ.*, 2009, **43**, 5853–5864.

71 M. Wesely, *Atmos. Environ.*, 1989, **23**, 1293–1304.

72 W. Gao and M. Wesely, *Atmos. Environ.*, 1995, **29**, 727–737.

73 J. A. Fisher, D. J. Jacob, Q. Wang, R. Bahreini, C. C. Carouge, M. J. Cubison, J. E. Dibb, T. Diehl, J. L. Jimenez, E. M. Leibensperger, Z. Lu, M. B. Meinders, H. O. Pye, P. K. Quinn, S. Sharma, D. G. Streets, A. van Donkelaar and R. M. Yantosca, *Atmos. Environ.*, 2011, **45**, 7301–7318.

74 L. Zhang, *Atmos. Environ.*, 2001, **35**, 549–560.

75 J. Scurlock, *Worldwide historical estimates of leaf area index, 1932-2000*, Oak Ridge National Lab (ORNL), Oak Ridge, TN, USA, technical report, 2002.

76 M. Li, Y. Wang and W. Ju, *Adv. Atmos. Sci.*, 2013, **31**, 179–187.

77 M. Jiskra, J. E. Sonke, D. Obrist, J. Bieser, R. Ebinghaus, C. L. Myhre, K. A. Pfaffhuber, I. Wängberg, K. Kyllönen, D. Worthy, et al., *Nat. Geosci.*, 2018, **11**, 244–250.

78 L. Zhang, G. Zhang, P. Zhou and Y. Zhao, *Bull. Environ. Contam. Toxicol.*, 2022, **110**, 16.

79 V. Shah, D. J. Jacob, C. P. Thackray, X. Wang, E. M. Sunderland, T. S. Dibble, A. Saiz-Lopez, I. Černušák, V. Kellö, P. J. Castro, R. Wu and C. Wang, *Environ. Sci. Technol.*, 2021, **55**, 14445–14456.